

Hydrogen in methanol catalysts by neutron imaging

Terreni, Jasmin; Billeter, Emanuel; Sambalova, Olga; Liu, Xiaochun; Trottmann, Matthias; Sterzi, Andrea; Geerlings, Hans; Trtik, Pavel; Kaestner, Anders; Borgschulte, Andreas

DOI

[10.1039/d0cp03414b](https://doi.org/10.1039/d0cp03414b)

Publication date

2020

Document Version

Final published version

Published in

Physical Chemistry Chemical Physics

Citation (APA)

Terreni, J., Billeter, E., Sambalova, O., Liu, X., Trottmann, M., Sterzi, A., Geerlings, H., Trtik, P., Kaestner, A., & Borgschulte, A. (2020). Hydrogen in methanol catalysts by neutron imaging. *Physical Chemistry Chemical Physics*, 22(40), 22979-22988. <https://doi.org/10.1039/d0cp03414b>

Important note

To cite this publication, please use the final published version (if applicable).
Please check the document version above.

Copyright

Other than for strictly personal use, it is not permitted to download, forward or distribute the text or part of it, without the consent of the author(s) and/or copyright holder(s), unless the work is under an open content license such as Creative Commons.

Takedown policy

Please contact us and provide details if you believe this document breaches copyrights.
We will remove access to the work immediately and investigate your claim.


 Cite this: *Phys. Chem. Chem. Phys.*,
2020, 22, 22979

Hydrogen in methanol catalysts by neutron imaging

 Jasmin Terreni,^{*ab} Emanuel Billeter,^{id ab} Olga Sambalova,^{id ab} Xiaochun Liu,^{ab}
Matthias Trottmann,^{ab} Andrea Sterzi,^{ab} Hans Geerlings,^c Pavel Trtik,^d
Anders Kaestner^{id d} and Andreas Borgschulte^{id ab}

Although of pivotal importance in heterogeneous hydrogenation reactions, the amount of hydrogen on catalysts during reactions is seldom known. We demonstrate the use of neutron imaging to follow and quantify hydrogen containing species in Cu/ZnO catalysts *operando* during methanol synthesis. The steady-state measurements reveal that the amount of hydrogen containing intermediates is related to the reaction yields of CO and methanol, as expected from simple considerations of the likely reaction mechanism. The time-resolved measurements indicate that these intermediates, despite indispensable within the course of the reaction, slow down the overall reaction steps. Hydrogen–deuterium exchange experiments indicate that hydrogen reduction of Cu/ZnO nano-composites modifies the catalyst in such a way that at operating temperatures, hydrogen is dynamically absorbed in the ZnO-nanoparticles. This explains the extraordinary good catalysis of copper if supported on ZnO by its ability to act as a hydrogen reservoir supplying hydrogen to the surface covered by CO₂, intermediates, and products during catalysis.

 Received 26th June 2020,
Accepted 19th September 2020

DOI: 10.1039/d0cp03414b

rsc.li/pccp

1 Introduction

The production of methanol from syngas is an established chemical process utilized on an industrial scale using highly efficient Cu/ZnO nanocatalysts.¹ With the advent of a worldwide renewable energy scenario, the production of methanol from CO₂ and renewable hydrogen is receiving increasing attention.^{2,3} This reaction is catalyzed by similar catalysts.⁴ Although long known, the reaction mechanism, in particular, the intermediates and relevance of the complex and the very specific nano-structure of the catalysts are debated.^{5,6} Recently, a careful structural analysis of such industrial Cu/ZnO catalysts triggered the hypothesis that zinc oxide has the ideal reducibility to catalyze methanol synthesis, which was found to be a consequence of the stability of the Cu/ZnO nanocomposite with the right bulk defects, and peculiar interface and surface structures.⁵ The authors concluded that the functioning of the methanol catalyst “could be further evaluated if a method

of quantitatively relating the reducibility to the catalytic properties could be found.”⁷ Traditionally, reducibility is experimentally assessed by the temperature programmed reduction (TPR) method, in which the amount of hydrogen consumed and its temperature dependence to reduce the previously oxidized catalyst is determined. This method depends on many experimental factors, which can strongly vary.¹ An elegant way of using model systems was introduced by Karim *et al.*⁸ The study emphasizes the strong link between the reducibility of the support and hydrogen spillover. The challenge of all experimental methods is the determination of the exact amount and dynamics of hydrogen in/on the material during reactions.⁹ As hydrogen has only one electron, its detection by analytical tools based on the interaction with electrons is challenging: core-level spectroscopies such as X-ray photoelectron spectroscopy¹⁰ and X-ray absorption^{11,12} cannot be used as a quantitative method for hydrogen, and hydrogen is nearly invisible for X-ray diffraction.^{13,14} A reliable probe must thus make use of the interaction with the proton, which is possible by nuclear magnetic resonance^{15,16} and neutron techniques. We demonstrate in this paper the use of neutron imaging to follow the number of hydrogen species *operando*. The interaction of neutrons with many types of materials is relatively weak,¹⁷ and thus, for example, a neutron beam can easily penetrate thick aluminum walls of a chemical reactor. Parallel to this, neutrons have a large cross-section with hydrogen, *i.e.*, we can probe hydrogen in an operating chemical reactor.¹⁸ Neutron imaging

^a University of Zurich, Department of Chemistry, Winterthurerstrasse, 190, CH-8057 Zurich, Switzerland

^b Empa, Swiss Federal Laboratories for Materials Science and Technology, Laboratory for Advanced Analytical Technologies, Überlandstrasse 129, CH-8600 Dübendorf, Switzerland. E-mail: andreas.borgschulte@empa.ch

^c Delft University of Technology, Department of Chemical Engineering, 2629 HZ Delft, The Netherlands

^d Laboratory for Neutron Scattering and Imaging (LNS), Paul Scherrer Institut (PSI), CH-5232 Villigen PSI, Switzerland

allows the quantification of the absolute amount of hydrogen containing compounds on a catalyst over the course of the reaction,¹⁹ and by relating to the surface area, the number of occupied sites is estimated. A drawback of the method is that it cannot provide information on which exact molecule is adsorbed. There are various possibilities: chemisorbed hydrogen, OH-groups, intermediates, and the products, water and methanol.^{20,21} We shed light on this uncertainty by simultaneously measuring the product yield as a function of partial pressures, temperatures and time by gas IR-analysis. The amount of mobile hydrogen on/in a catalyst is determined by neutron imaging of hydrogen–deuterium exchange. In addition, we support the neutron experiments by laboratory experiments making use of the weight change upon hydrogen–deuterium exchange. The main outcome of the experiments is that the hydrogen reduction of Cu/ZnO nano-composites modifies the catalyst in such a way that at operating temperatures, hydrogen is dynamically absorbed. This explains the extraordinary good catalysis of copper if supported by ZnO by its ability to act as a hydrogen reservoir supplying hydrogen to the surface covered by CO₂, intermediates, and products during catalysis.

2 Experimental

2.1 Samples

Commercial copper-based methanol synthesis catalyst Cu/ZnO/Al₂O₃ pellets were purchased from Alfa Aesar. Catalytic performance: maximum methanol yield at *ca.* 225 °C and 12 bar is around 12 g MeOH (kg cat)⁻¹ h⁻¹; space velocity = 60 000 h⁻¹.

X-ray diffraction (XRD) patterns were obtained using a PANalytical X'Pert-Pro powder X-ray diffractometer, using Cu K α monochromatized radiation (1.541 Å) in the range of $2\theta = 10\text{--}90^\circ$ (X-ray gun setting at 40 kV and 40 mA).

The XRD powder pattern of the studied catalyst (Fig. 2) shows broad diffraction lines corresponding to monoclinic CuO (ICDD-PDF 16025) and ZnO (ICDD-PDF 26170). Crystalline rosasite (CuZn)₂CO₃ (ICDD-PDF 109166) as well as graphite (ICDD-PDF 76767) are identified and the low infrared reflectivity of the samples is explained (see DRIFTS discussion below). Interestingly, we do not observe peaks related to alumina, which is thus X-ray amorphous. These observations are in good agreement with the ones found for similar Cu/ZnO/alumina catalysts as studied in ref. 22 and 23.

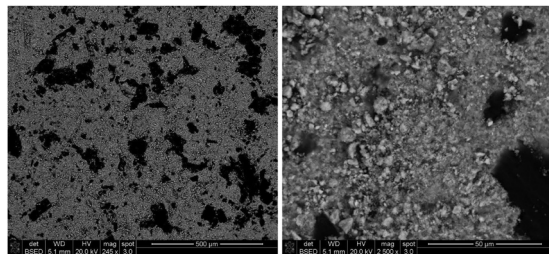


Fig. 1 Scanning electron microscopy images of the catalysts at two different magnifications. The black spots are identified as empty space.

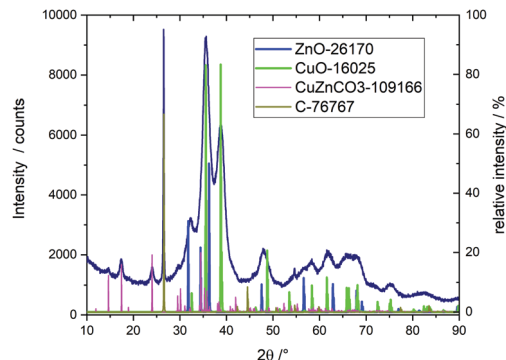


Fig. 2 X-ray diffraction pattern of the Cu/ZnO/alumina catalyst.

2.2 Surface characterization

The total surface area determined by BET (micrometrics ASAP 2000) was found to be 105 m² g⁻¹. The copper surface area was determined using hydrogen reduction/N₂O oxidation cycles.²⁴ The freshly reduced catalyst is exposed to N₂O. Simultaneously, the weight change is recorded and normalized by the atomic weight of oxygen and the total weight of the sample. Assuming that only the two uppermost atomic layers of the Cu nanoparticles are oxidized, *i.e.* [Cu]/[O] = 1,²² one can relate the weight change to the number of Cu surface atoms giving a Cu surface area of 18 m² g⁻¹, in good agreement with the literature.²² Experimental conditions: Rubotherm magnetic suspension balance, Rubotherm Bochum, reducing in H₂ at 300 °C, cooling down to 100 °C, He for 1 h, N₂O for 30 min, He for 1 h.

2.3 Neutron imaging

High-resolution neutron imaging was performed at the cold neutron beamline ICON²⁵ at the Swiss Neutron Spallation Source (SINQ), PSI (Switzerland).²⁶ The SINQ neutron source is operated at 1.33 mA delivering polychromatic neutrons in the thermal to cold energy range. The beam defining aperture at ICON beamline was 20 mm in diameter and the imaging detector was placed at the measuring position no. 2. The collimation ratio (L/D) was equal to approximately 350. After traversing the sample position, the neutron beam was captured using a 20 µm thick gadolinium oxysulfide scintillator screen. The scintillation light has been collected using a fibre optics taper (FOT)²⁷ in contact with the scintillator screen by its small end. The light emitted from the large end of the FOT has been detected using a standard camera box (MIDI box) using a 100 mm Zeiss Makro-Planar objective and a 2048 × 2048 charged couple device (Andor Technology). The resulting pixel size of the acquired images was equal to 6.2 micrometres and the spatial resolution, assessed visually by imaging the Siemens star test pattern,²⁸ was equal to approximately 20 micrometres. The sample (Cu/ZnO pellet) was placed in a heated reactor cell made of aluminum, near to the scintillator plate at around 20 mm distance, and aligned to have the pellet's cylindrical axis parallel to the neutron beam. The exposure time of the individual neutron images was equal to 20 s. For measurements

under static conditions, 10 images were averaged for better statistics. The image analysis was performed using software ImageJ using built-in functions and a plug-in for image normalization developed by the Neutron Imaging and Applied Materials Group at PSI.

The total neutron attenuation coefficient σ_{tot} was calculated using the sum of total neutron scattering cross-section (coherent plus incoherent) and the neutron absorption coefficient.¹⁷ With the setup used for neutron imaging (thermal neutrons with broad energy range), the attenuation coefficients do not depend significantly on the chemical nature of the species.²⁹

2.4 Gas supply and analysis

The gas (reactants) flows were controlled by using thermal mass flow meters from Bronkhorst connected to a Labview interface. Typical flow rates were 25 mL min⁻¹ CO₂, and 100 ml min⁻¹ H₂ (and deuterium, respectively). The product gases were led through an FTIR-gas cell installed in a Bruker Alpha spectrometer acquiring spectra at a resolution of 0.8 cm⁻¹. Gravimetric analysis was performed using a Rubotherm magnetic suspension balance (Bochum, Germany) attached to the same gas supply system.³⁰

Diffusive reflectance infrared Fourier transform spectra (DRIFTS) were collected using a Vertex 70 infrared spectrometer (Bruker Optics) equipped with a DRIFT unit (Praying Mantis, Harrick) and a liquid nitrogen cooled MCT detector. The commercial Harrick cell (HVC-DRP-3) was attached to the same gas manifold system used for neutron imaging (see above).

DRIFTS has already been used to identify the main reactants, intermediates, and products adsorbed on the surface as well as in the gas phase during CO₂ reduction on Cu/ZnO–alumina.^{32,33} However, due to the high carbon content and various nano-crystalline materials (see Fig. 2), the infrared reflectivity of the sample is extremely low, and the observed changes originate mainly from reactants and products in the gas phase. Furthermore, bulk phases such as rosasite (CuZn(OH)₂(CO₃)) may influence the DRIFTS signal, if they are modified during the reduction/reaction.

3 Results and discussion

Fig. 4 explains the idea of neutron imaging for catalysis along experimental neutron images of an industrial methanol catalyst consisting of a pellet with 5.4 mm diameter and 3.6 mm height (see photo). The pellet is inserted into a heated aluminum reactor. The neutron beam is attenuated while travelling through the sample/sample holder. With 1.7 barn,^{17,34} the total neutron attenuation coefficient (see the Experimental section) for aluminum is low, but not negligible. Thus, the bore of the reactor is visible on a neutron transmission image as a brighter area (Fig. 4). The total neutron attenuation coefficient for Cu (11.81 barn) and Zn (5.24 barn) is higher,¹⁷ and thus the catalyst pellet placed inside the bore appears as a black disk. This image serves as the reference image (= reference signal I_0). During the reaction, the gas content as well as adsorbed species

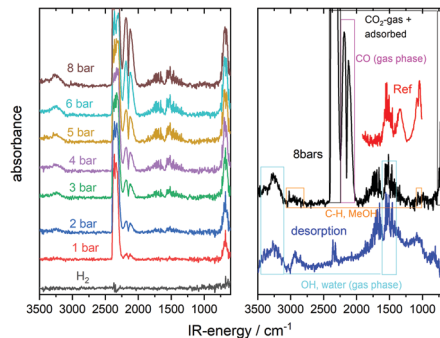


Fig. 3 DRIFTS experiments on a Cu/ZnO/Alumina catalyst hydrogen/CO₂ mixture (1 : 3) up to 8 bar. The panel highlights the 8 bar spectrum, and the one after stopping CO₂ flux showing remaining adsorbates. The reference spectrum (at 1 bar H₂/CO₂) is taken from ref. 31.

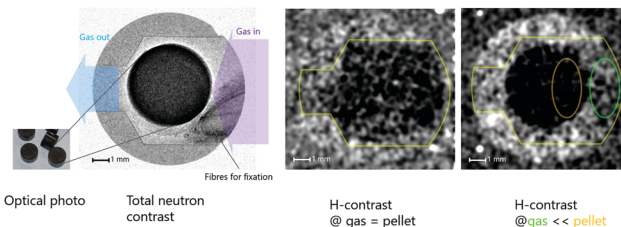


Fig. 4 Neutron transmission image of a Cu/ZnO catalyst pellet (optical photo on the left) placed in an aluminum reactor (left large picture). Middle and right pictures show the neutron contrast image under different conditions, one with hardly any excess hydrogen adsorption in the catalyst, (middle), and one with marked adsorption in the catalyst exceeding that of the gas phase (right). The contrast is maximized for each image for better visibility. The yellow line is a guide to the eyes to indicate the reactor bore.

changes. Possible elements are hydrogen, oxygen and carbon with absorption cross-sections of 82.35 barn, 4.23 barn, and 5.55 barn, respectively.¹⁷ Effectively any changes of the neutron attenuation can thus be related to the changes of the number of hydrogen atoms. The changes of the hydrogen content x_{H} are recorded as a deviation from the reference image $I_{t=0}/I_0$. This deviation is quantified by applying the Lambert–Beer law:

$$\ln\left(\frac{I_0}{I}\right) = x_{\text{H}} \cdot d \cdot \mu \quad (1)$$

where d is the thickness of the disk, μ is the molar cross-section. This approach is possible because the neutrons transmit the sample in the direction of the pellet's cylinder axis. Fig. 4 shows two typical examples: one, in which hydrogen adsorption in the sample is negligible also at high hydrogen gas pressure, and one with high hydrogen load in the sample.

In the first case, the sample is exposed to H₂ at higher pressure than that used while taking the background image. Due to the increased number of hydrogen atoms in the gas phase, the whole bore appears as a dark area. In this particular case, as there is no significant difference (contrast) with the pellet area, one can conclude that the amount of hydrogen in the gas phase is similar to the amount of hydrogen species on the catalyst. In the second case, the catalyst is exposed

simultaneously to CO₂ and H₂ (reaction conditions). Under these particular conditions, hydrogen containing species accumulate on the surface of the catalyst. These additional species lead to a comparably higher contrast at the pellet area compared to the gas phase. To separate the signals originating from gas and hydrogen in the catalyst, the gas signal is subtracted from the signal in the pellet, which contains both contributions, giving the “excess hydrogen” in the catalyst $x_{\text{H}} \propto \ln(I_{\text{cat}}/I_{\text{gas}})$. For experimental details, see the Experimental section.

3.1 Excess hydrogen during catalysis

The excess hydrogen plotted as a function of CO₂ concentration in Fig. 5 shows the number of protons associated with the material. It may become negative as is the case for a lower temperature at 0% CO₂, and indicates that the number of hydrogen atoms in the catalyst's volume is smaller than in the free gas space. These hydrogen atoms may be hydrogen attached to the surface, including –OH species and –H on ZnO^{35,36} as well as hydrogen chemisorbed on Cu,^{20,37} which then transform into reaction intermediates and products, such as formate, acetal, and methoxy species^{21,32,38} as well as water and methanol,³⁸ respectively. Neutron imaging as utilized here (white neutrons in the thermal energy range) cannot distinguish between differently bound hydrogens.³⁹ However, the larger amount of excess hydrogen at finite CO₂ concentration is a consequence of the circumstance that the number of hydrogen atoms per adsorbate after the reaction is higher than the ones formed in pure hydrogen. In the latter case, we expect only chemisorbed hydrogen (H*) and hydroxide (OH*), while during the reaction hydrogen rich compounds are formed, e.g., HCOOH*, H₂CO*, H₃CO*, H₃COH* + H₂O* (see the discussion mechanism below). This hypothesis is further corroborated by the concentration dependence: the plateau-like behavior indicates that the reaction species are formed nearly independent of the actual gas concentration and reaction yield (compare simultaneously measured CO- and methanol-yield in Fig. 5, particularly at 448 K). This indicates that the surface coverage consists mainly of inactive, possibly even inhibiting

adsorbates. Further evidence for this is given by time dependence of the process.

Time dependent measurements (Fig. 6) show that the complete removal, *i.e.*, the desorption of intermediates and products from the surface takes up to one hour after switching from high pressure reaction conditions to pure hydrogen at 1 bar, while the coverage is completed within a few minutes after switching to reaction conditions. The main desorption product is water. Interestingly, also the methanol concentration peaks with pressure release, in contrast to CO, which just stops. Micro-kinetic models³⁸ emphasize the stability of some intermediates (such as OH forming eventually water, see below) on the surface of the catalyst blocking adsorption sites needed for catalysis. This explains the initial higher production yield as well as the absence of a concentration dependence of the coverage: a few percent of CO₂ is sufficient to produce these adsorbates covering most of the surface of the catalyst.

Further insights into the chemistry taking place during catalysis may be concluded by comparison of the results with the ones supported by spectroscopic methods such as inelastic neutron scattering (INS)^{40–42} and diffusive reflectance infrared Fourier transform spectroscopy (DRIFTS).^{32,33} DRIFTS is a true *operando* spectroscopy, *i.e.*, it is compatible with the particular sample form (usually powder) and sample environment (gas, liquid) at elevated temperatures and pressures.⁴³ However, the signals of the adsorbed as well as gaseous molecules depend on the IR-reflectivity of the catalyst.^{44–46} Concretely, DRIFTS on ‘black’ (no-IR reflectivity) catalysts is very challenging.⁴⁷ We performed DRIFTS measurements (see the Experimental section), but did not obtain meaningful information on surface adsorbates due to the extremely low infrared reflectivity of the sample.

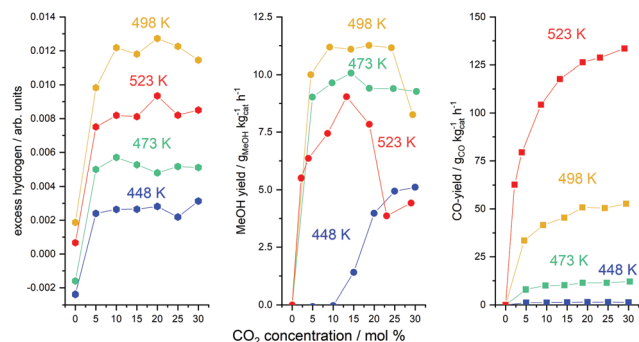


Fig. 5 Left graph: “Excess hydrogen” $x_{\text{H}} \propto \ln(I_{\text{cat}}/I_{\text{gas}})$ at 12 bar hydrogen as a function of the CO₂ concentration and temperature. Simultaneously, the MeOH-yield (middle graph) and CO-yield are determined (right graph). For the CO-yield, Arrhenius analysis gives an activation energy of $E_{\text{A}} = 1.24$ eV (≈ 120 kJ mol⁻¹).

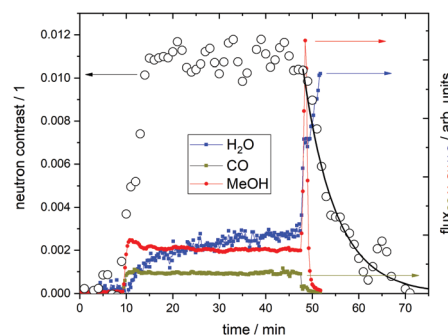
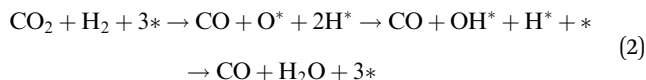
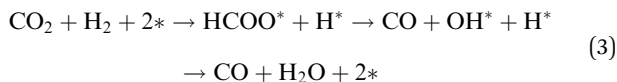


Fig. 6 Time resolved *operando* measurements: the neutron contrast as parameter of the amount of hydrogen containing adsorbates on the catalyst surface reaches steady-state rapidly after switching from H₂ to H₂/CO₂ mixtures as does the CO-yield. Contrarily, the MeOH yield has a maximum on the fresh sample, and the water signal slowly increases. Switching off CO₂ and reducing the pressure to ambient conditions forces desorption of intermediates and products. The immediate decrease of the CO signal indicates that there is only little CO adsorbed, while the increase of MeOH and water proves that a substantial amount of MeOH-related intermediates and the products themselves are adsorbed as also visible by the rather slow decay of the neutron contrast (the line is a fit to an exponential function). Reaction conditions: $p = 12$ bar, $T = 473$ K, and H₂:CO₂ ratio = 6:1.

From literature experiments and DFT-modelling³⁸ the following reaction mechanisms were proposed (for illustration, see Fig. 9): CO-production proceeds *via* the reverse water gas shift (RWGS) reaction *via* a dissociative mechanism:^{37,48,49}

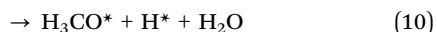
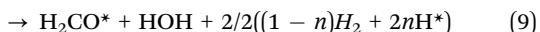
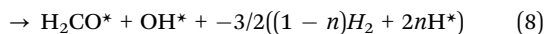
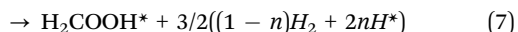
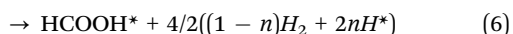
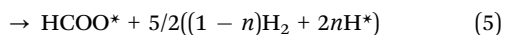


or *via* the associative mechanism:⁵⁰



The dissociative mechanism is often called “redox” mechanism, which stems from the fact that there is an electron transfer involved from CO₂ to the adsorption site * to form chemisorbed oxygen O*. On Cu, this corresponds to the oxidation of Cu⁰ to Cu^I. The role of hydrogen would then be to reduce the oxidized Cu back to Cu⁰.⁴⁸ In principle, the first reaction step of the associative mechanism may proceed *via* Langmuir–Hinshelwood or *via* an Eley–Rideal pathway, possibly even concurrently as has been suggested for the RWGS on nickel.⁴⁹ However, for copper, there is strong experimental evidence that formate formation proceeds *via* the Eley–Rideal pathway, in which only hydrogen is chemisorbed at the surface, and CO₂ reacts from the gas phase or physisorbed state.⁵⁰

A crucial difference between processes 2 and 3 is the additional hydrogen containing intermediate (formate) that is formed during the associative pathway. In both reactions, water is formed and its reaction from OH* and H* is slow³⁸ and thus the overall reaction yield is reduced. It is evident that the CO reaction yield depends on the partial pressure of CO₂ and hydrogen and on the temperature to overcome the activation barrier,³⁷ as observed (Fig. 5). The measured yields and an Arrhenius analysis derived activation energy of approximately 1.24 eV (120 kJ mol⁻¹) are in good agreement with those of earlier studies ($E_A = 1.6$ eV (150 kJ mol⁻¹)⁵¹). In contrast, for the reduction of CO₂ to methanol at least six hydrogen containing species (HCOO*, HCOOH*, CH₃O₂*, CH₂O*, OH*, and CH₃O*) are formed on the surface of the catalyst according to the most probable pathway:³⁸



where n is the relative amount of hydrogen chemisorbed on the surface to that left in the gas phase. Without the reservoir of intermediates, methanol cannot be formed, which is in very

good agreement with our experiment: highest methanol yield is found at the highest amount of excess hydrogen. The lack of substantially adsorbed CO suggests an explanation of the need for CO₂ for CO hydrogenation to methanol: even if direct pathways³⁸ may be available, the surface is covered by stronger binding adsorbates such as CO₂ and water. The neutron experiments are thus in agreement with the hypothesis that production of CO from CO₂ takes place *via* the associative pathway, although the results are not decisive.

The first step of the methanol synthesis and the associative mechanism of the RWGS reaction share formate as a common intermediate. Both reactions share another reaction step: the hydrogenation of OH* to form H₂O* and its subsequent desorption (eqn (9)), which has a high barrier.³⁸ However, the formation of CO depends on the partial pressure of CO₂, which rapidly decreases if the CO₂ supply is stopped (Fig. 6). *Vice versa*, methanol formation continues and the yield is even increased due to the enhanced reaction of the still present intermediates with adsorbed hydrogen. Simultaneously, the water formation is markedly increasing, which continues even after the complete reaction towards methanol. This is in line with the hypothesis that adsorbates such as OH* block the chemisorption of hydrogen for reactions with CO₂, methanol intermediates and with OH* itself. This fact is formally taken into account by introducing the variable n in the formulae (4)–(11), indicating that the ratio of chemisorbed hydrogen to hydrogen in the gas phase (n) is unknown. Various studies showed that hydrogen adsorption/desorption on Cu is fast compared to the synthesis rates of methanol.¹⁵ Hydrogen coverages of up to 40% at 10 bar were calculated. It is obvious, though, that chemisorbed hydrogen competes with other adsorbates for the same surface sites. Askgaard *et al.* provided detailed values based on a micro-kinetic model:⁵² at 50 bar and 500 K, the coverage by hydrogen $\theta_{\text{H}^*} = 0.330$ is significantly larger than that of all other adsorbates: $\theta_{\text{HCOO}^*} = 0.070 > \theta_{\text{CH}_3\text{CO}^*} = 0.042 > \theta_{\text{OH}^*} = 0.017 > \theta_{\text{CO}^*} = 0.016 > \theta_{\text{CO}_2^*} = 0.0028 > \theta_{\text{H}_2\text{O}^*} = 0.0017 \gg \theta_{\text{rest}}$. However, below this temperature, HCOO* is the most abundant species, with $\theta_{\text{HCOO}^*} \simeq 1$ eventually blocking all free sites. Thus, the high calculated rates of hydrogen chemisorption on Cu are existent as long as further reactions with this chemisorbed hydrogen and eventually desorption of the formed intermediates are guaranteed.¹⁵ The neutron data (excess hydrogen in Fig. 5) confirm experimentally that the surface is quickly equilibrated with additional hydrogen containing intermediates including water, which will reduce the hydrogen chemisorption rate.

In principle, the method gives absolute numbers. The number of hydrogen atoms per volume at 4 bar partial hydrogen pressure corresponds to $N_{\text{H}}/V = 2.6 \times 10^{26} \cdot 4 / (24 \times 10^{-3}) \text{ m}^{-3} \simeq 2 \times 10^{29} \text{ m}^{-3}$. The surface area is 105 m² g⁻¹ (see the Experimental section), the density is around 5 g cm⁻³, and the total surface atom density is around 1.46×10^{19} atoms per m². This gives the number of surface atoms per volume $N_{\text{surf}}/V = 2 \times 10^{29} \text{ m}^{-3}$. If we now measure a hydrogen excess of 0.01, we can estimate that 1% of the surface are covered by new species. Approximately 1/6 of the surface consists of Cu atoms (see the Experimental section). The order of coverage is in good

agreement with the numbers discussed above.⁵² This estimation can be further specified using reference samples and/or reference states of the sample to be performed in the future.

Recently, a crucial difference between methanol synthesis from CO and hydrogen and methanol from CO₂ has been found and traced back to the fact that only in the latter reaction water is formed and adsorbed at the surface and thereby blocking reaction sites.⁵³ The results at hand, both neutron imaging (Fig. 6) as well as DRIFTS, showing water as the only identifiable adsorbate (Fig. 3), corroborate this finding. The active removal of the product water is thus expected to enhance the reaction yield. This idea, also called sorption enhanced catalysis, was recently experimentally demonstrated (Cu/ZnO catalyst in ionic liquids,⁵⁴ and Cu/zeolite catalyst⁵⁵).

3.2 Hydrogen on/in Cu/ZnO

The concentration of H* under methanol synthesis conditions is pivotal but cannot be measured easily due to interference with other hydrogen containing species. We have therefore studied the behavior of the catalyst in the absence of CO₂. To further increase the accuracy of our experiments, we combined neutron imaging with hydrogen–deuterium exchange. The hydrogen flow to the sample, which has been equilibrated at a given temperature and pressure, is abruptly exchanged for deuterium under the same conditions and later back to hydrogen again. Deuterium has a considerably lower neutron attenuation coefficient ($\sigma_{\text{tot}}(D) = 7.64$ barn, compared to $\sigma_{\text{tot}}(H) = 82.35$ barn),¹⁷ and thus the neutron contrast ($\ln I_D - \ln I_H$) is directly proportional to the amount of hydrogen, which can be dynamically exchanged. With this technique, we can follow the kinetic measurements on the time scale of seconds (Fig. 7).

An advantage of the neutron technique is the imaging possibility, giving insights into diffusion processes. In zeolite based catalysts, we could show by this technique that macroscopic diffusion controls the reaction rate in catalyst pellets,¹⁹ a very well-known constraint in technical catalysts.⁵⁶ However, on the accessible time and length scale of the experiments

applied here, no differences of the time evolution at the outer and inner parts of the catalyst pellets are observed (Fig. 7). This indicates that the time dependence of the process stems from microstructural modifications, and the macroscopic transport through the pellet is too fast to be captured by neutron imaging with experimental parameters used. This conclusion is further corroborated by scanning electron microscopy images depicting the highly porous structure of the technical catalyst with voids of several 100 micrometer sizes (Fig. 1). On the other hand, the temporally accessible changes take place on length scales, which are not resolved by neutron imaging (below a micrometer). To still yield some insights into the atomistic changes, we only studied the time- and temperature dependence of the averaged hydrogen content on/in the catalyst.

With neutron imaging being a very expensive technique, we highlight here a complimentary possibility for probing the H/D exchange. As the mass of deuterium is twice that of hydrogen, the exchange of hydrogen can be gravimetrically determined (for details of the apparatus, see ref. 30). However, the Cu/ZnO/Al₂O₃ catalyst is not stable in hydrogen, it loses weight even after long equilibration (2 hours, see Fig. 7), which is attributed to the loss of oxygen by reduction of the ZnO. If now the hydrogen gas in the reactor is rapidly exchanged by deuterium, a steep weight increase is observed indicative of exchange of hydrogen by deuterium in the sample. By reversing the process, the same negative weight difference is obtained. We compare the H/D exchange experiments using a magnetic suspension balance with the results from neutron imaging in Fig. 7. Steep changes upon gas changes (from hydrogen to deuterium and *vice versa*) are observed by both techniques and the rapid reversible exchange of hydrogen in Cu/ZnO is observed. The difference to the neutron measurements is that in addition to mass changes from H/D exchange mass changes occur from desorption of adsorbates and oxygen. This is visible by the linear decrease of the weight on top of the rapid changes. Still, by deduction this continuous change, the neutron contrast can be calibrated against the weight changes (compare also Fig. 8). In absolutely pure hydrogen, Cu/ZnO is unstable, and oxygen desorbs from the catalyst. This process starts around 450 K as usually determined by TPR.⁵⁷ The degree of reduction depends on the oxygen partial pressure. At temperatures below 800 K, only the surface of Cu/ZnO nano-catalysts is reduced,²⁰ if practical hydrogen (deuterium) purities are used; the threshold oxygen partial pressure of $p_{\text{O}_2} = 10^{-10}$ mbar corresponds to 13N hydrogen, which is technically unrealistic. We can thus assume that the main part of the catalyst remains as ZnO, and only Cu, the direct vicinity of ZnO and its surface are reduced, as supported by numerous other studies^{5,58} on Cu/ZnO (for enlightening discussion see Nakamura *et al.*⁵⁹).

An unexpected result is the increase of the maximum hydrogen content (maximum H/D exchange) with temperature. This is observed both by neutron imaging as well by gravimetric analysis (Fig. 8). This additional weight change, which is practically subtracted from the sought signal, demonstrates that the hydrogen adsorption on the catalyst is coupled to the reduction of it. The observation of increasing hydrogen content

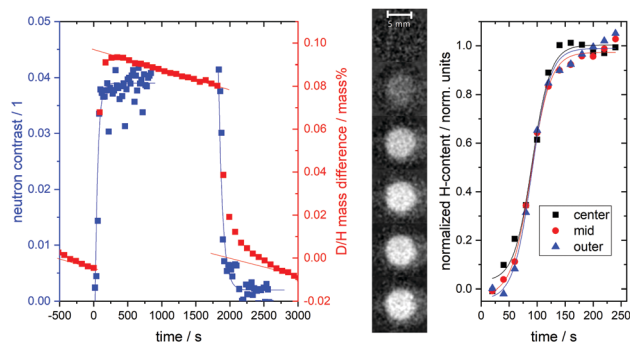


Fig. 7 Left graph: Change of neutron contrast and mass of the Cu/ZnO/Al₂O₃ catalyst upon gas switch from hydrogen to deuterium and *vice versa* at 200 °C. Right graph: Time- and spatially-resolved neutron contrast upon hydrogen deuterium exchange (at $t = 0$) derived from the neutron radiography image series ($t = 0, 25, 50, 75, 100,$ and 250 s) at three different locations in the pellet (in the center, at half radius and at maximum radius).

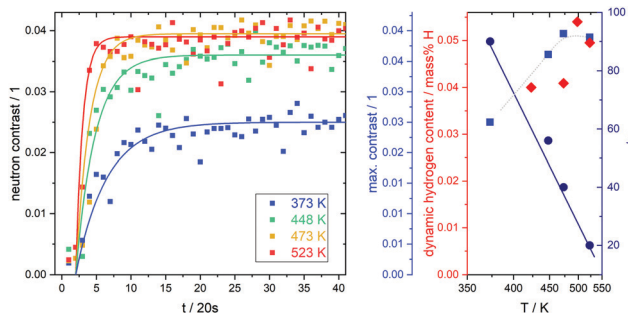


Fig. 8 Left panel shows the neutron contrast upon hydrogen–deuterium exchange in the Cu/ZnO/Al₂O₃ catalyst at various temperatures yielding the kinetics of hydrogen mobility and total amount of hydrogen expressed by the amplitude (maximum contrast, blue squares) and time constant (dark blue spheres) derived from an exponential fit to the data, respectively. An Arrhenius analysis of the time constant (right panel) gives an activation energy of $E_A = 0.16$ eV. The maximum neutron contrast is compared to gravimetric H–D exchange measurements (red diamonds) calibrating the absolute amount of hydrogen in the sample.

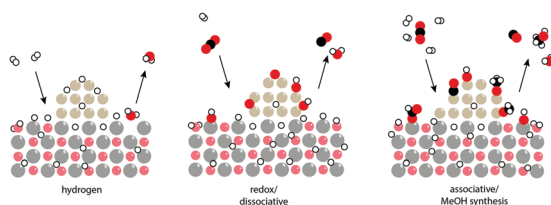


Fig. 9 Left panel: A sketch of a Cu/ZnO catalyst in pure hydrogen gas. Hydrogen is adsorbed on Cu and on ZnO, as well as absorbed in ZnO and to a minor extent in Cu. There is consensus in the literature that the Cu/Zn interface is metallic.⁵ Catalyst reduction includes the partial removal of oxygen by water formation as well. Middle and right panel: Cu/ZnO during catalysis. The main difference is that the surface is covered with reactants, intermediates, and products, and thus diffusion of hydrogen *via* the bulk becomes relevant. The positioning of the molecules is speculative. The middle panel sketches CO formation *via* the redox mechanism (2) and the right one displays CO and methanol formation *via* the associative pathway *via* HCOO* (3).

with increasing temperature is counterintuitive: one expects a typical hydrogen ad/absorption curve⁶⁰ with the negative (exothermic) heat of adsorption and thus highest coverage is expected to occur at lowest temperature. Examples may be the

well-known dissociative adsorption of H₂ on Cu,^{61,62} while infrared studies unveiled the active sites for this dissociative adsorption of H₂ on pure ZnO as pairs of Zn and O surface atoms.³⁵ With $x \simeq 0$, the driving force for hydrogen uptake is the entropy gain, and then ΔH may be positive, too (Sieverts law):^{63,64}

$$x_H \propto \sqrt{\frac{p}{p_0}} e^{-\frac{\Delta H_H}{k_B T} + \Delta S_H} \quad (12)$$

Such a behavior is observed in bulk absorption of hydrogen, *i.e.*, ΔH_H and ΔS_H are the enthalpy and entropy of solution, respectively.

With this background information, it is possible to specify the kind of hydrogen on/in Cu/ZnO, being hydrogen adsorbed on the surface, or absorbed in the bulk. Following Table 1, hydrogen absorbed in ZnO is the most likely candidate matching the condition of a positive heat of absorption as well as a relatively high amount. The H-increase is evidenced by H/D exchange probed by neutron imaging as well as mass changes (Fig. 7); the observed mass loss at these temperatures indicates that also oxygen leaves the catalyst. The latter is evidence for some degree of surface reduction, as significant bulk reduction is expected at much higher temperatures only. In contrast to TPR-methods, neutron imaging together with gravimetric analysis allows the separation of these two components of reducibility of a catalyst (hydrogen absorption and oxygen removal), which is usually assessed only by one parameter, hydrogen consumption.

Hydrogen absorption in ZnO is a well-known phenomenon; ZnO is a wide bandgap semiconductor with peculiar opto-electronic properties, which change upon hydrogen insertion.^{65–69} An important question arises, whether this bulk hydrogen is relevant in catalysis. The kinetic measurements show an exponential behavior. We derived a time constant τ from an exponential fit to the kinetic curves (Fig. 8). With increasing temperature, the equilibrium is reached faster. An Arrhenius analysis gives an activation energy of $E_A = 0.16$ eV. Hydrogen dissociation on copper is activated with a barrier height of 1 eV.⁷⁰ First-principles electronic structure calculations predict a barrier height of $E_D \simeq 0.4$ eV for the bulk diffusion of hydrogen in ZnO,^{68,69} *i.e.*, the transport of hydrogen from

Table 1 Hydrogen in and on Cu/ZnO. For visualization of the various sites, see Fig. 9

Reaction	Formula	Heat of reaction	Est. Amount
Surface adsorption	$\frac{1}{2} \text{H}_2 + \text{Cu} \rightarrow \text{Cu} \cdot \text{H}$,	$\Delta H_{(\text{Cu})\cdot\text{H}} = -39 \text{ kJ mol}^{-1}$ ⁶⁰	2×10^{-2} mass%
Bulk absorption	$\frac{1}{2x} \text{H}_2 + \text{Cu} \rightarrow \text{CuH}_x$,	$\Delta H_{\text{CuH}_x} = +48 \text{ kJ mol}^{-1}$ H ⁷⁶	1×10^{-7} mass% ⁷⁶
Surface adsorption	$\frac{1}{2} \text{H}_2 + \text{ZnO} \rightarrow (\text{ZnO}) \cdot \text{H}$,	$\Delta H_{(\text{ZnO})\cdot\text{H}} < 0$	5×10^{-2} mass%
Bulk absorption	$\frac{1}{2x} \text{H}_2 + \text{ZnO} \rightarrow \text{ZnOH}_x$,	$\Delta H_{\text{ZnOH}_x} > 0$	2×10^{-1} mass% ⁶⁷
Surface reduction	$\frac{3}{2} \text{H}_2 + \text{ZnO} \rightarrow \text{Zn} \cdot \text{H} + \text{H}_2\text{O}$	$\frac{2}{3}(-\Delta H_{\text{ZnO}} + \Delta H_{\text{H}_2\text{O}} + \Delta H_{\text{Zn}\cdot\text{H}}) > 0$	$x_H \simeq 0$, $\Delta m/M = -8.6$ mass%
Bulk reduction	$\text{H}_2 + \text{ZnO} \rightarrow \text{Zn} + \text{H}_2\text{O}$	$-\Delta H_{\text{ZnO}} + \Delta H_{\text{H}_2\text{O}} > 0$	$x_H \simeq 0$, $\Delta m/M = -20$ mass%

dissociation sites on the surface *via* the bulk of the ZnO-nanoparticles to the reaction sites at the Cu–Zn interface is likely. One empirical indication is that the total hydrogen uptake reaches its maximum, where the reaction yield towards methanol has its maximum. *Operando* neutron imaging shows a high amount of reaction intermediates and water, which block ‘ordinary’ hydrogen dissociation and chemisorption (Fig. 6) suggesting that hydrogen supply in methanol synthesis over Cu/ZnO catalysts is facilitated by spillover from ZnO to Cu, as suggested by Spencer *et al.*¹⁵ The special ‘promoter effect’ of ZnO and other ‘reducible’ oxides such as In₂O₃ may thus be simply explained by the possibility of fast hydrogen transport through the bulk of the nano-support. This interpretation is in line with recent results on doped ZnO:⁷¹ if the doping led to enhanced conductivity, catalytic activity is found to increase. As discussed above, hydrogen insertion increases the conductivity.^{65–69}

Various studies identified a peculiar nanostructure of Cu as well as ZnO and thus interface between Cu and ZnO formed during reduction and/or reaction as the reactive sites.^{5,6,72} The findings of this study add an additional explanation of its relevance: it is straightforward to relate the overall catalytic activity to the surface area, as the number of potentially active sites scales with it. In addition, bulk diffusion can only be relevant to heterogeneous catalysis, if the diffusion path lengths are very short of the order of a few nanometer limiting the effect to nm-sized structures. This is in line with experiments of Nakamura *et al.*⁷³ and Studt *et al.*,⁷⁴ who found that that already small amounts of Zn below the detection limit for bulk-ZnO are sufficient to promote Cu nano-particles. Bulk hydrogen should thus be understood in the sense of sub-surface hydrogen. Further synergistic effects between Cu and Zn as suggested by the aforementioned papers are very likely, too, but cannot be studied by the methods utilized in this paper.

4 Conclusions

Using neutron imaging we are able to follow and quantify hydrogen containing species in Cu/ZnO during methanol synthesis. The steady-state measurements reveal that the amount of hydrogen containing intermediates is related to the reaction yields of CO and methanol, as expected from simple considerations of the likely reaction mechanism. The time-resolved measurements indicate that these intermediates, despite indispensable within the course of the reaction, slow down the overall reaction steps. A disadvantage of neutron imaging is the lack of further chemical information other than the total amount of hydrogen. In combination with the product gas analysis, DRIFTS, and the literature, we show that water is one of the main adsorbates. The measurement of the total neutron scattering under operating conditions supported subsequently by INS on the same sample quenched to INS-compatible measurements^{40,41,75} may be a future combination to overcome the experimental limitations of each individual

method. In addition to hydrogen containing species during the reaction, we probe the amount of hydrogen in the catalyst in pure hydrogen by H/D exchange. The analysis brings to the fore that a considerable amount of hydrogen is mainly located in the bulk of the ZnO nanoparticles, while traditionally “catalyst reduction” is associated with the removal of oxygen by water formation during hydrogen exposure at high temperatures. As hydrogen can be rapidly exchanged in the catalyst, we propose that this absorbed hydrogen is relevant for catalysis *via* spillover to the active sites at the Cu/Zn interfaces, and not only a spectator. Although it was not intended, the difficulty in using DRIFTS on the same samples shows the robustness of the method, which has no experimental constraints like optical reflectivity limiting the use of DRIFTS and other optical *operando* methods.

Author contributions

J. T., E. B., O. S., A. S., A. B., A. K., and P. T. performed the neutron imaging experiments, X. L. and M. T. performed the characterisation of the catalysts, H. G. contributed to the analysis of the experiments, A. B. and P. T. defined and designed the concept of neutron imaging for catalysis, and all authors contributed to the writing of the study.

Conflicts of interest

There are no conflicts to declare.

Acknowledgements

This work was partly supported by the UZH-UFSP program LightChEC. Financial support from the Swiss National Science Foundation (grant no. 144120 and 172662) is acknowledged.

References

- 1 I. Chorkendorff and J. Niemantsverdriet, *Concepts of Modern Catalysis and Kinetics*, Wiley-VCH Verlag GmbH & Co. KGaA, New York, 2007.
- 2 G. A. Olah, A. Goepfert and G. K. S. Prakash, *Beyond Oil and Gas: The Methanol Economy*, Wiley-VCH Verlag GmbH & Co. KGaA, Heidelberg, 2009.
- 3 B. Patterson, *et al.*, *Proc. Natl. Acad. Sci. U. S. A.*, 2019, **116**, 12212–12219.
- 4 M. D. Porosoff, B. Yan and J. G. Chen, *Energy Environ. Sci.*, 2016, **9**, 62.
- 5 M. Behrens, *Science*, 2012, **759**, 893.
- 6 C. Tisseraud, C. Comminges, S. Pronier, Y. Pouilloux and A. Le Valant, *J. Catal.*, 2016, **343**, 106–114.
- 7 J. P. Greeley, *Science*, 2012, **336**, 810.
- 8 W. Karim, C. Spreafico, A. Kleibert, J. Gobrecht, J. VandeVondele, Y. Ekinici and J. A. van Bokhoven, *Nature*, 2017, **541**, 68–71.

- 9 T. Y. Wei, K. Lim, Y. S. Tsenga and S. L. I. Chan, *Renewable Sustainable Energy Rev.*, 2017, **79**, 1122–1133.
- 10 L. Nguyen, F. F. Tao, Y. Tang, J. Dou and X.-J. Bao, *Chem. Rev.*, 2019, **119**, 6822–6905.
- 11 M. A. Newton and A. J. Dent, in *In situ Characterization of Heterogeneous Catalysts*, ed. J. A. Rodriguez, J. C. Hanson and P. J. Chupas, Energy-Dispersive EXAFS: Principles and Application in Heterogeneous Catalysis, John Wiley and Sons Inc, New Jersey, 2013, pp. 75–119.
- 12 J. A. van Bokhoven and C. Lamberti, in *XAFS Techniques for Catalysts, Nanomaterials, and Surfaces*, ed. Y. Iwasawa, K. Asakura and M. Tada, XAS Techniques to Determine Catalytically Active Sites in Zeolites: The Case of Cu-Zeolites, Springer International Publishing, Cham, 2017, pp. 299–316.
- 13 H. Cheng, C. Lu, J. Liu, Y. Yan, X. Han, H. Jin, Y. Wang, Y. Liu and C. Wu, *Prog. Nat. Sci.: Mater. Int.*, 2017, **27**, 66–73.
- 14 F. Buchter, Z. Lodziana, A. Remhof, P. Mauron, O. Friedrichs, A. Borgschulte, A. Züttel, Y. Filinchuk and L. Palatinus, *Phys. Rev. B: Condens. Matter Mater. Phys.*, 2011, **83**, 064107.
- 15 M. S. Spencer, *Catal. Lett.*, 1998, **50**, 37.
- 16 L. Bouchard, S. Burt, M. S. Anwar, K. V. Kovtunov, I. V. Koptug and A. Pines, *Science*, 2008, **319**, 442.
- 17 V. F. Sears, *Neutron News*, 1992, **3**, 26.
- 18 A. Borgschulte, R. Delmelle, R. B. Duarte, A. Heel, P. Boillat and E. Lehmann, *Phys. Chem. Chem. Phys.*, 2016, **18**, 17217.
- 19 J. Terreni, M. Trottmann, R. Delmelle, A. Heel, P. Trtik, E. H. Lehmann and A. Borgschulte, *J. Phys. Chem. C*, 2018, **122**, 23574–23581.
- 20 L. Martinez-Suarez, J. Frenzel, D. Marx, B. Meyer and L. Marti, *Phys. Rev. Lett.*, 2013, **110**, 086108.
- 21 S. Dang, H. Yang, P. Gao, H. Wang, X. Li, W. Wei and Y. Sun, *J. Catal.*, 2013, **330**, 61.
- 22 P. Kurr, I. Kasatkin, F. Girgsdies, A. Trunschke, R. Schlögl and T. Ressler, *Appl. Catal., A*, 2008, **348**, 153–164.
- 23 B. Liang, J. Ma, X. Su, C. Yang, H. Duan, H. Zhou, S. Deng, L. Li and Y. Huang, *Ind. Eng. Chem. Res.*, 2019, **58**, 9030–9037.
- 24 M.-J. Luys, P. van Oeffelt, P. Pieters and R. Ter Veen, *Catal. Today*, 1991, **10**, 283–292.
- 25 A. Kaestner, *et al.*, *Nucl. Instrum. Methods Phys. Res., Sect. A*, 2011, **659**, 387–393.
- 26 B. Blau, K. N. Clausen, S. Gvasalaliya, M. Janoschek, S. Janssen, L. Keller, B. Roessli, J. Scheffer, P. Tregenna-Piggott, W. Wagner and O. Zaharo, *Neutron News*, 2009, **20**, 5.
- 27 M. Morgano, P. Trtik, M. Meyer, E. H. Lehmann, J. Hovind and M. Strobl, *Opt. Express*, 2018, **26**, 1809–1816.
- 28 C. Grünzweig, G. Frei, E. Lehmann, G. Kühne and C. David, *Rev. Sci. Instrum.*, 2007, **78**, 053708.
- 29 S. C. Capelli and G. Romanelli, *J. Appl. Crystallogr.*, 2019, **52**, 1233–1237.
- 30 A. Borgschulte, F. Pendolino, R. Gremaud and A. Züttel, *Appl. Phys. Lett.*, 2009, **94**, 111907.
- 31 X. Wang, H. Zhang and W. Li, *Korean J. Chem. Eng.*, 2010, **27**, 1093–1098.
- 32 I. A. Fisher and A. T. Bell, *J. Catal.*, 1997, **172**, 222.
- 33 Y. Wang, S. Kattel, W. Gao, K. Li, P. Liu, J. G. Chen and H. Wang, *Nat. Commun.*, 2019, **10**, 1166.
- 34 P. C. H. Mitchell, S. F. Parker, A. J. Ramirez-Cuesta and J. Tomkinson, *Vibrational Spectroscopy with Neutrons With Applications in Chemistry, Biology, Materials Science and Catalysis*, World Scientific Publishing, Singapore, 2005.
- 35 G. L. Griffin and J. T. Yates, *J. Chem. Phys.*, 1982, **77**, 3744.
- 36 J. Kiss, A. Witt, B. Meyer and D. Marx, *J. Phys. Chem.*, 2009, **130**, 184706.
- 37 K. H. Ernst, C. T. Campbell and G. Moretti, *J. Catal.*, 1992, **134**, 66.
- 38 L. C. Grabow and M. M. Mavrikakis, *ACS Catal.*, 2011, **1**, 365.
- 39 J. Biesdorf, P. Oberholzer, F. Bernauer, A. Kaestner, P. Vontobel, E. H. Lehmann, T. J. Schmidt and P. Boillat, *Phys. Rev. Lett.*, 2014, **112**, 248301.
- 40 T. Kandemir, M. Friedrich, S. F. Parker, F. Studt, D. Lennon, R. Schlögl and M. Behrens, *Phys. Chem. Chem. Phys.*, 2016, **18**, 17353.
- 41 I. P. Silverwood, N. G. Hamilton, C. J. Laycock, J. Z. Staniforth, R. M. Ormerod, C. D. Frost, S. F. Parker and D. Lennon, *Phys. Chem. Chem. Phys.*, 2010, **12**, 3102–3107.
- 42 I. P. Silverwood, N. G. Hamilton, A. McFarlane, R. M. Ormerod, T. Guidi, J. Bones, M. P. Dudman, C. M. Goodway, M. Kibble, S. F. Parker and D. Lennon, *Rev. Sci. Instrum.*, 2011, **82**, 034101.
- 43 T. Armaroli, T. Bécue and S. Gautier, *Oil Gas Sci. Technol.*, 2004, **59**, 215–237.
- 44 P. Kubelka and F. Munk, *Z. Tech. Phys.*, 1931, **12**, 593–601.
- 45 P. Kubelka, *J. Opt. Soc. Am.*, 1948, **38**, 448–457.
- 46 L. H. Little, *Infrared Spectra of Adsorbed Species*, Academic Press, NewYork, 1966, pp. 1933–1941.
- 47 J. J. Venter and M. A. Vannice, *Carbon*, 1988, **26**, 889–902.
- 48 C. Chen, W. Cheng and S. Lin, *Catal. Lett.*, 2000, **68**, 45–48.
- 49 W. Lin, K. M. Stocker and G. C. Schatz, *J. Am. Chem. Soc.*, 2017, **139**, 4663–4666.
- 50 J. Quan, F. Muttaqien, T. Kondo, T. Kozarashi, T. Mogi, T. Imabayashi, Y. Hamamoto, K. Inagaki, I. Hamada, Y. Morikawa and J. Nakamura, *Nat. Chem.*, 2019, **11**, 722–729.
- 51 K. Kobl, S. Thomas, Y. Zimmermann, K. Parkhomenko and A.-C. Roger, *Catal. Today*, 2016, **270**, 31–42.
- 52 T. S. Askgaard, J. N. Norskov, C. V. Ovesen and P. Stoltze, *J. Catal.*, 1995, **156**, 229.
- 53 A. V. Tarasov, F. Seitz, R. Schlögl and E. Frei, *ACS Catal.*, 2019, **9**, 5537–5544.
- 54 J. Reichert, S. Maerten, K. Meltzer, A. Tremel, M. Baldauf, P. Wasserscheid and J. Albert, *Sustainable Energy Fuels*, 2019, **3**, 3399–3405.
- 55 J. Terreni, M. Trottmann, T. Franken, A. Heel and A. Borgschulte, *Energy Technol.*, 2019, **7**, 1801093.
- 56 E. W. Thiele, *Ind. Eng. Chem.*, 1939, **31**, 916–920.
- 57 J. C. Slaa, G. J. M. Weierink, J. G. van Ommen and J. R. H. Ross, *Catal. Today*, 1992, **12**, 481.
- 58 S. Kattel, P. J. Ramirez, J. G. Chen, J. A. Rodriguez and P. Liu, *Science*, 2017, **355**, 1296.
- 59 J. Nakamura, T. Fujitani, S. Kuld, S. Helveg, I. Chorkendorff and J. Sehested, *Science*, 2017, **357**, 6354.
- 60 K. Christmann, *Surf. Sci. Rep.*, 1988, **7**, 1.
- 61 K. W. Frese, *Surf. Sci.*, 1987, **182**, 85.

- 62 P. B. Rasmussen, P. M. Holmblad, H. Christoffersen, P. A. Taylor and I. Chorkendorff, *Surf. Sci.*, 1992, **287–288**, 79.
- 63 A. Borgschulte, R. Gremaud and R. Griessen, *Phys. Rev. B: Condens. Matter Mater. Phys.*, 2008, **78**, 094106.
- 64 N. Lopez, Z. Lodziana, F. Illas and M. Salmeron, *Phys. Rev. Lett.*, 2004, **93**, 146103.
- 65 C. G. Van de Walle, *Phys. Rev. Lett.*, 2000, **85**, 1012–1015.
- 66 C. G. Van de Walle and J. Neugebauer, *Nature*, 2003, **423**, 626–628.
- 67 G. Brauer, W. Anwand, D. Grambole, J. Grenzer, W. Skorupa, J. Cizek, J. Kuriplach, I. Prochazka, C. C. C. Ling, K. So, D. Schulz and D. Klimm, *Phys. Rev. B: Condens. Matter Mater. Phys.*, 2009, **79**, 115212.
- 68 M. G. Wardle, J. P. Goss and P. R. Briddon, *Phys. Rev. Lett.*, 2006, **96**, 205504.
- 69 H.-H. Nahm, C. H. Park and Y.-S. Kim, *Sci. Rep.*, 2014, **4**, 4124.
- 70 B. E. Hayden and C. L. A. Lamont, *Phys. Rev. Lett.*, 1989, **63**, 1823–1825.
- 71 J. Schumann, M. Eichelbaum, T. Lunkenbein, N. Thomas, M. C. Álvarez Galván, R. Schlögl and M. Behrens, *ACS Catal.*, 2015, **5**, 3260–3270.
- 72 R. van den Berg, G. Prieto, G. Korpershoek, L. I. van der Wal, A. J. van Bunningen, S. Laegsgaard-Joergensen, P. E. de Jongh and K. P. de Jong, *Nat. Commun.*, 2016, **7**, 13057.
- 73 J. Nakamura, I. Nakamura, T. Uchijima, T. Watanabe and T. Fujitani, in *Model studies of methanol synthesis on copper catalysts*, ed. J. W. Hightower, W. N. Delgass, E. Iglesia and A. T. Bell, *Studies in Surface Science and Catalysis*, Elsevier, 1996, vol. 101, pp. 1389–1399.
- 74 F. Studt, M. Behrens, E. L. Kunkes, N. Thomas, S. Zander, A. Tarasov, J. Schumann, E. Frei, J. B. Varley, F. Abild-Pedersen, J. K. Nørskov and R. Schlögl, *ChemCatChem*, 2015, **7**, 1105–1111.
- 75 J. Terreni, O. Sambalova, S. Borgschulte, A. Rudić, S. Parker and A. Ramirez-Cuesta, *Catalysts*, 2020, **10**, 433.
- 76 H. Magnusson and F. Frisk, *J. Phase Equilib. Diffus.*, 2017, **38**, 65–69.